Photonics-Assisted Wideband RF Source Localization Method Based on Synthetic Aperture Interferometric Detection

Yue Yang, Jiewen Ding, Cong Ma, Fengting Cao, Xiangchuan Wang, and Shilong Pan, *Senior Member, IEEE, Fellow, OSA*

***Abstract*—Angle of arrival (AOA) is one key parameter for passive signal source localization. However, with the increase in RF systems' instantaneous bandwidth and working frequency, it is a great challenge for traditional narrowband array signal processing methods to achieve effective AOA measurement of wideband RF sources. This paper proposes a photonics-assisted wideband RF source localization method based on synthetic aperture interferometer radiometer (SAIR) detection. The proposed method introduced cross-power spectrum (CPS), which can characterize the interference at different frequencies to define the wideband visibility function. Then the wideband SAIR detection is achieved from the wideband visibility function, which is Fourier transformed in the spatial domain and then performs integration in the frequency domain. Numerical simulation and proof-of-concept experiment results show that the proposed method can suppress the grating lobes caused by large element spacing. With a microwave photonic (MWP) channelizer and an antenna array, a wideband signal covering 16–20 GHz is detected. The AOA resolution of the system is 3.54°, and the power of the maximum grating lobe in the AOA measurement is suppressed by over 80%.**

***Index Terms*—Angle of arrival, interferometric radiometer, microwave photonics, passive detection, wideband array.**

I. Introduction

PASSIVE detection technology is widely used in many fields, such as wireless communication, electronic warfare, radio astronomy, and airborne/space-borne remote sensing [1]. Compared with active detection methods such as active radar, a passive detection system does not need to transmit any electromagnetic energy, which has excellent concealment and anti-interference ability. In addition, with the shortage of frequency spectrum resources, passive detection without occupied frequency bands has become one of the key technologies for integrated sensing and communication (ISAC) in 6G [2], [3]. Angle-of-arrival (AOA) that can characterize targets' location is an essential parameter in passive detection. However, with the demand for high-speed communication and high-resolution detection, AOA detection systems must be able to process RF signals with a large instantaneous bandwidth over a frequency range up to tens of gigahertz, which is challenging for traditional electronic technologies.

Compared with electronic-based methods, microwave photonics (MWP) based systems have significant advantages such as large operating bandwidth, low transmission loss, and anti-electromagnetic interference [4]–[8]. In recent years, many MWP-based AOA measurement methods have been proposed [9]–[17]. One typical class of these methods is based on AOA-power mapping. For example, an approach to estimate AOA through optical power measurement is proposed [9]. By interfering with the sidebands corresponding to each replica of the RF signals at the optical carrier wavelength, the phase difference of two replicas of the RF signals is converted to the optical power at the optical carrier. The AOA can then be calculated from the total power at the carrier wavelength. Similar AOA measurement methods based on power detection, such as the optical sideband power [10], output microwave signal power [11], or DC voltage [12], are proposed. However, the AOA result will be coupled with the power of the incoming signal, and a power calibration procedure should be performed in advance. A parallel structure base on a dual polarization modulator is presented to address this [13]. Another AOA measurement method is proposed based on optical phase scanning [14]. The AOA of both single-frequency signal at 10 GHz and wideband signal from 17 to 19 GHz can be measured by scanning the phase of the optical sideband and processing the output low-frequency signal.

These AOA measurement systems mentioned above are based on a simple architecture consisting of two antennas and cascaded or composite modulators. However, many modern communication and radar systems are now implemented based on antenna arrays with N (N>2) elements, which can obtain higher signal gain as well as spatial resolution. So it is necessary to study the MWP-based AOA measurement method combined with a large-scale array. A photonics-based AOA estimation method

Manuscript received 4 June 2022; revised 31 July 2022; accepted 5 August 2022. Date of publication 8 August 2022; date of current version 3 October 2022. This work was supported in part by the National Natural Science Foundation of China under Grant 62075095 and in part by the Natural Science Foundation of Jiangsu Province under Grant BK20180066. *(Corresponding authors: Xiangchuan Wang; Shilong Pan.)*

The authors are with the Key Laboratory of Radar Imaging and Microwave Photonics, Ministry of Education, Nanjing University of Aeronautics and Astronautics, Nanjing 210016, China (e-mail: yangyue96@nuaa.edu.cn; dingjw@nuaa.edu.cn; cmaxc@nuaa.edu.cn; cfting@nuaa.edu.cn; wangxch@nuaa.edu.cn; pans@nuaa.edu.cn).

Color versions of one or more figures in this article are available at https://doi.org/10.1109/JLT.2022.3197289.

Digital Object Identifier 10.1109/JLT.2022.3197289

using phased-array antennas is presented [15], where the AOA of the wideband signal can be derived from the free-spectral range (FSR) of the system output frequency response. A compressive sensing-assisted photonic AOA measurement algorithm is presented in [16], where a better estimation accuracy and robustness than the traditional power detection-based method is achieved. Apart from these works based on simulation or semi-physical simulation experiments, some research is implemented with actual antenna arrays. We have proposed and experimentally demonstrated a photonics-assisted passive array detection system based on the principle of synthetic aperture interferometric radiometer (SAIR) in [18]. The AOA of two incoherent RF sources can be estimated in the target detection experiment. A space-optics-based SAIR system is proposed in [19] and [20]. By applying optical up-converting, the RF wavefront captured by the antenna array is transferred to the optical wavefront, and the AOA of multiple targets can be solved quickly. This method simplifies the hardware complexity of the SAIR system by using lens optics.

However, the principle of AOA measurement in these systems is still based on the narrowband array signal processing method assuming that the ratio of element spacing to signal wavelength is constant. In that case, the value of element spacing is usually set to half of the signal wavelength to avoid grating the lobe. Since MWP-based RF systems usually need to process signals with large instantaneous bandwidth, where the narrowband assumption is no longer valid. If the element spacing is set to half of the minimum wavelength, more array elements and receivers need to be added, resulting in increased production difficulty and system cost. Therefore, it is necessary to investigate a SAIR detection method for wideband RF source detection as large element spacing could be inevitable in a sense.

In this paper, we have proposed a passive array detection method for wideband RF signal sources location. An experiment demonstration combined with a microwave photonic channelizer is then carried out to verify the feasibility and performance of the proposed method. The rest of this paper is organized as follows. Section II gives a brief introduction to the narrowband SAIR system, followed by the proposed wideband SAIR concept and measurement method. In Section III, a microwave photonic channelizer based wideband RF signal AOA array detection system is built for proof-of-concept experiments. The AOA measurement of both single and double wideband RF sources is successfully implemented. Section IV gives some discussion and conclusion.

II. Principle

A. Synthetic Aperture Interferometric Radiometer

The principle of the traditional SAIR system is based on the Van Cittert-Zernike theorem [21], [22]. When the far-field condition is met, the visibility function is the spatial Fourier transform of the intensity distribution of target RF sources. The schematic diagram of the geometric relationship of the theorem is shown in Fig. 1. In narrowband conditions, the

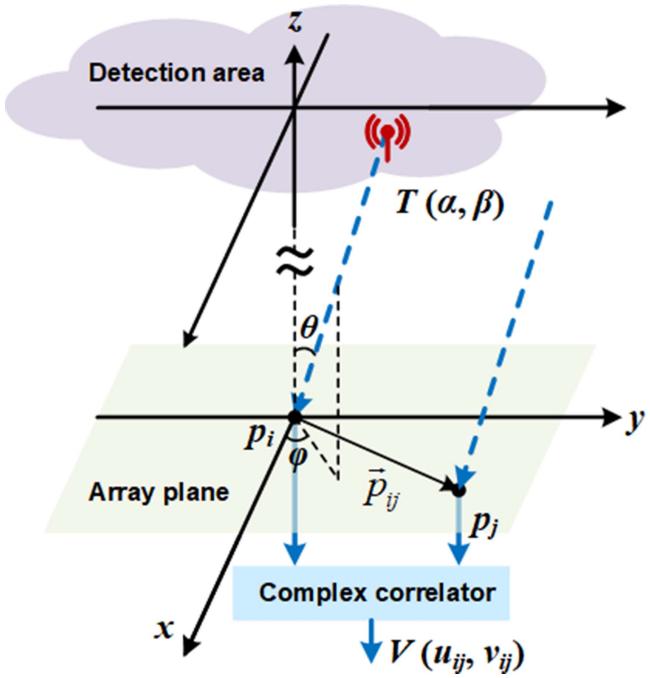

Fig. 1. Schematic diagram of the geometric relationship of Van Cittert-Zernike theorem.

Van Cittert-Zernike theorem can be expressed in the following form

$$T(\alpha,\beta)=\int\int V(u_{ij},v_{ij})\exp\left[j2\pi\left(u_{ij}\alpha+v_{ij}\beta\right)\right]dudv \tag{1}$$

where $T(\alpha, \beta)$ is the far field 2-D spatial scene intensity distribution to be measured, $\alpha = \sin\theta\cdot\cos\varphi$, $\beta = \sin\theta\cdot\sin\varphi$ are the direction cosines in Cartesian coordinate with respect to the x-axis and y-axis. The visibility function $V(u, v)$ is the complex correlation function with zero time offset between signals received by two different elements in the array, which can be written as

$$\begin{aligned} V(u_{ij},v_{ij}) &= \left\langle s_i(t)\cdot s_j^*(t)\right\rangle \\ &= \lim_{T\to\infty}\frac{1}{T}\int_{-\infty}^{\infty}S_i(\omega)\cdot S_j^*(\omega)d\omega \end{aligned} \tag{2}$$

where $s_i(t)$ is the signal received by the ith antenna, $S_i(\omega)$ is the corresponding frequency spectrum, $\langle\cdot\rangle$ represents a time average operation, and T is the accumulation time of the received signal. For the baseline vector $\vec{p}_{ij}$ consisting of antenna $p_i(x_i, y_i)$ and $p_j(x_j, y_j)$ in Fig. 1, the spatial frequencies can be written as $u_{ij} = |x_i\text{-}x_j|/\lambda_{\mathrm{RF}}$ and $v_{ij} = |y_i\text{-}y_j|/\lambda_{\mathrm{RF}}$, here λ_{RF} is the center frequency of the received signal. However, only discrete samples of the visibility function can be acquired in practical array systems. The theorem should be represented in discrete form.

$$T(\alpha,\beta)=\sum_i\sum_j\left\{V(u_{ij},v_{ij})\exp\left[j2\pi\left(u_{ij}\alpha+v_{ij}\beta\right)\right]\right\} \tag{3}$$

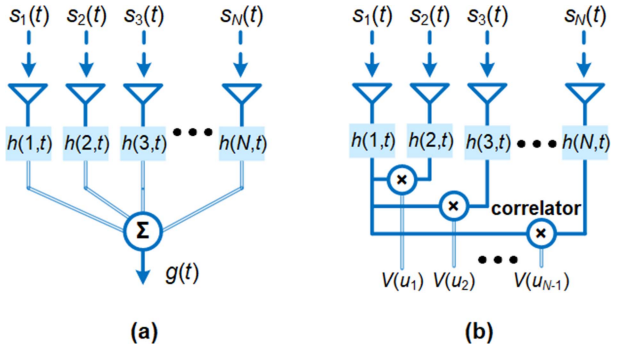

Fig. 2. Comparison between a beamforming system in receive mode (a) and a SAIR system(b).

By collecting the visibility function of different baselines in the *u*-*v* plane, the scene intensity distribution in the far-field can be calculated by the Fourier transform in (3).

B. Wideband Synthetic Aperture Interferometric Radiometer Based on Cross Power Spectrum and Frequency Integration

An important assumption in the Van Cittert-Zernike theorem is that the receiver's bandwidth should be much smaller than the center frequency [22]. Therefore, the principle of the traditional SAIR system mentioned above is valid only under narrowband conditions. If the target is a wideband RF source, the narrowband assumption no longer holds, i.e., the ratio of element spacing to the wavelength will change with the temporal frequency. It has been proved that there is a common mathematical framework for both synthetic aperture interferometry array and actual aperture array [23], so the wideband SAIR system can be modeled in a similar way to a wideband beamforming system [24]. To simplify the analysis, we consider the case in a 1-D array. Since the SAIR system is a passive detection system, we take an example of a wideband beamforming system in receive mode that does not need to transmit a signal. The schematic diagram of the beamforming system is depicted in Fig. 2(a). After different delays or phase shifts, signals received from different antennas in the array are superimposed to form an equivalent receiving beam in the spatial domain. The output signal of the beamforming system can be written as

$$g(t) = \sum_{n} \int_{-\infty}^{\infty} s_n(\tau) \cdot h(t-\tau)\, d\tau \tag{4}$$

where $s_n(t)$ is the signal received by the nth antenna, and $h_n(t)$ is the impulse response of the nth receive chain. According to [24], the 1-D array-based wideband beamforming network can be further equivalent to a 2-D spatial-temporal filter, and the output signal can be found as

$$g(n,t) = s(n,t) \otimes h(n,t)\,|_{n=0} \tag{5}$$

where the spatial index n is listed as another independent variable and $\otimes$ represents a 2-D convolution. The output can also be expressed using a 2-D spatial-temporary frequency response

$$\begin{aligned} G(\Omega,\omega) &= \sum_{n=1}^{N} \int_{-\infty}^{\infty} s(n,t) \otimes h(n,t)\, e^{-j(\omega t - n\Omega)} dt \\ &= \sum_{n=1}^{N} S(n,\omega) \cdot H(n,\omega)\, e^{j(n\Omega)} \end{aligned} \tag{6}$$

Where Ω is the spatial frequency. For a more intuitive representation, the output can be rewritten in angle-frequency (θ-ω) form as

$$\begin{aligned} G(\theta,\omega) &= \sum_{n=1}^{N} \int_{-\infty}^{\infty} s(n,t) \otimes h(n,t)\, e^{-j\left(\omega t - n\frac{\omega d}{c}\sin\theta\right)} dt \\ &= \sum_{n=1}^{N} S(n,\omega) \cdot H(n,\omega)\, e^{j\left(n\frac{\omega d}{c}\sin\theta\right)} \end{aligned} \tag{7}$$

where d is the spacing between two adjacent elements in the uniform linear array, c is the speed of light in the vacuum, and θ is the observation angle in the far-field of the array. Considering the whole signal frequency band, the integrated antenna pattern (IAP) [25] is then used to calculate the spatial scene intensity distribution in the far field. The IAP is obtained by integrating the response data on different frequencies components at a given spatial angle

$$\begin{aligned} IAP(\theta) &= \int_{-\pi B}^{\pi B} |G(\theta,\omega)|^2\, d\omega \\ &= \int_{-\pi B}^{\pi B} \left| \sum_{n=1}^{N} S(n,\omega) \cdot H(n,\omega)\, e^{j\left(n\frac{\omega d}{c}\sin\theta\right)} \right|^2 d\omega \end{aligned} \tag{8}$$

where B is the bandwidth of the signal. When it comes to a SAIR system shown in Fig. 2(b), we can equivalent the calculation of the far-field intensity distribution to that of the antenna pattern in the beamforming system. The 1-D spatial scene intensity distribution can be written as

$$T(\theta) = \sum_{n=1}^{N-1} \left[V(u_n) \exp(j2\pi u_n \sin\theta) \right] \tag{9}$$

For better understanding, it is assumed that the array of the SAIR system is the same 1-D uniform linear array as the beamforming system mentioned above. The sample of visibility function $V(u_n)$ is defined as the cross-correlation between the 1st and n+1th element in the array. When a wideband RF signal is detected, the intensity distribution $T(\alpha)$ and visibility function $V(u)$ should become a function of frequency:

$$T(\theta,\omega) = \sum_{n=1}^{N-1} \left[V(u_n,\omega) \exp(j2\pi u_n \sin\theta) \right] \tag{10}$$

However, the visibility function defined in (2) is the average of all frequency components within the receiver bandwidth. The spatial frequency variation with the temporal frequency corresponding to the same baseline is ignored, so it is not suitable for wideband scenarios. The cross-power spectrum (CPS) based

AOA estimation method has been applied in passive sonar systems [26] with large relative bandwidth. Since it can characterize the cross-correlation result at each frequency, we introduce a CPS-based visibility function for wideband RF source detection.

$$V(u_n,\omega)=\lim_{T\to\infty}\frac{1}{T}\left[S_1(\omega)S_{n+1}^{*}(\omega)\right] \tag{11}$$

Because the variable $u_n = n\omega d/c$ is related to the other variable ω, in order to make both variables independent, we can rewrite (11) as the following form

$$V(n,\omega)=\lim_{T\to\infty}\frac{1}{T}\left[S(1,\omega)S^{*}(n+1,\omega)\right] \tag{12}$$

Furthermore, to obtain distortion-free SAIR detection results, the impact of the frequency response of receive link should also be taken into account. The visibility function in equation (12) can be expressed as

$$V(n,\omega)=\lim_{T\to\infty}\frac{1}{T}\left[S_{\mathrm{R}}(1,\omega)H(1,\omega)\cdot S_{\mathrm{R}}^{*}(n+1,\omega)H^{*}(n+1,\omega)\right] \tag{13}$$

Here, $S_{\mathrm{R}}(n, \omega)$ is the signal measured at the antenna. Since the principle of the SAIR system is to measure the visibility function of the antenna signals, a calibration process is required to restore these signals from the measured ones. Therefore, (10) should be rewritten as

$$T(\theta,\omega)=\sum_{n=1}^{N-1}\left[\frac{V(n,\omega)}{H(1,\omega)H^{*}(n+1,\omega)}e^{j2\pi n\frac{\omega d}{c}\sin\theta}\right] \tag{14}$$

Then the wideband SAIR detection result can be calculated by integrating the SAIR detection result at different temporary frequencies, which is similar to the above-mentioned IAP in (8).

$$T(\theta)=\int_{-\pi B}^{\pi B}\sum_{n=1}^{N-1}\left[\frac{V(n,\omega)}{H(1,\omega)H^{*}(n+1,\omega)}e^{j2\pi n\frac{\omega d}{c}\sin\theta}\right]d\omega \tag{15}$$

For instance, consider an ideal 12-way SAIR system with a large working bandwidth. The element spacing of the uniform linear array is 2.46cm. Suppose a target RF source with a center frequency of 18 GHz and a bandwidth of 4 GHz is located in the far-field direction of $+15°$ of the array. The element spacing is about 1.48 times the wavelength at 18 GHz, which does not meet the half-wavelength condition required for the largest grating-lobe-free aperture. The AOA detection result is depicted in Fig. 3(a) with the solid blue line for the result obtained by the traditional narrowband SAIR detection method and the dashed orange line for the wideband SAIR detection method. The measured AOA is 14.96°, which is close to the set value. In addition to the main lobe corresponding to the target, there are two grating lobes in the result obtained by the traditional SAIR detection method. When the wideband SAIR detection method is applied, the grating lobes are significantly suppressed.

A two-target scenario is then simulated, with two target sources in the same frequency band as the previous single-target scenario placed in the direction of $-10°$ and $+15°$ of the array, respectively. The corresponding result is depicted in Fig. 3(b). The measured AOA results of the two targets are $-9.97°$ and 14.88° respectively. As can be seen, the number of grating lobes increases proportionally in the result of the traditional SAIR detection method, which will seriously affect the detection performance of the system. In contrast, the AOA result obtained by the wideband method shown in the dashed orange line will not suffer from this problem.

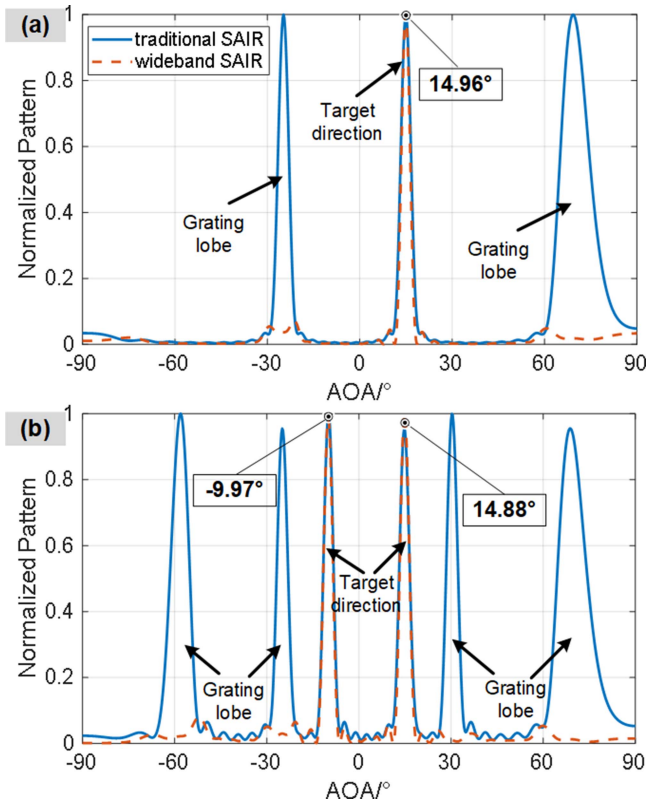

Fig. 3. Simulation result of traditional SAIR detection method and wideband SAIR detection method for single (a) and dual-target (b) cases.

III. Experiments and Results

A. System Structure

A proof-of-concept experiment is carried out combined with a microwave photonic channelizer based on a dual-output image-reject mixer [27] depicted in Fig. 4. A continuous-wave (CW) optical carrier at 1550.12 nm is generated by a laser diode (LD, NKT photonics KoherasBasiKX1) and divided into three branches through a 1×3 optical coupler (OC). In the upper branch, the CW light is modulated by a single-frequency microwave signal at a Mach-Zehnder Modulator (MZM1, Finisar FTM7938EZ). MZM1 is biased at the null point to suppress the optical carrier. The modulated optical signal is then filtered by an optical bandpass filter (OBPF) with the $+1^{st}$ sideband remaining. The output of OBPF is connected to the local oscillator (LO) port of two 90-degree optical hybrids via a 50:50 OC.

In the lower two branches, the optical carrier is sent to two MZM (MZM2 and MZM3) driven by signals collected by two different elements in the array. It should be noted that due to

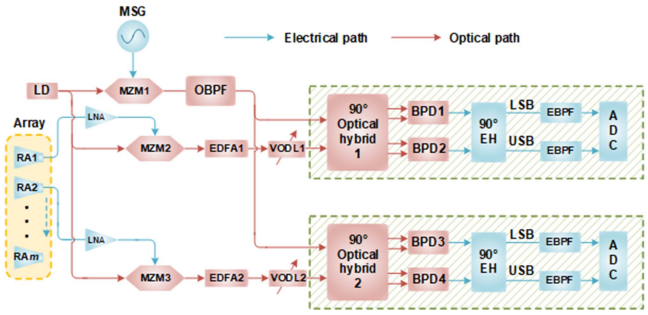

Fig. 4. Experimental setup of the microwave photonic channelizer. LD, laser diode, MZM, Mach-Zehnder modulator, MSG, microwave signal generator, OBPF, optical bandpass filter, EDFA, erbium-doped fiber amplifier, VODL, variable optical delay line, BPD, balanced photodetector, 90°EH, 90-degree electrical hybrid, LSB, lower sideband, USB, upper sideband, EBPF, electrical bandpass filter, ADC, analog-to-digital convertor, RA, receive antenna, LNA, low noise amplifier.

the hardware limitation, only two receive links can be built at the same time. Therefore, the AOA measurement is achieved by selecting the pairs of antennas with increasing spacing to synthesize an equivalent 1-D aperture. The samples of the visibility function are obtained by time division.

The outputs of the two MZMs in the lower branches are directed to an erbium-doped fiber amplifier (EDFA, Amonics AEDFA-PA-35-B-FA), respectively. The outputs of the EDFAs are connected to the RF port of two 90-degree optical hybrids via a variable optical delay line (VODL) used to compensate for the link delay difference. After the optical hybrid, two balanced photodetectors (BPD) are applied for optical-to-electronic conversion. The generated electronic signals are combined at a 90-degree electronic hybrid with two electrical bandpass filters (EBPF, passband: 0.5–1.5GHz) connected to remove the out-of-band signals. The frequency components located at the lower and upper of the LO can be output at the same time.

B. RF Channelization

RF channelization experiment is first conducted. A wideband linear frequency modulated (LFM) signal covering 16–20 GHz with a positive chirp slope is applied to the microwave photonic channelizer. The period of the target LFM signal is 2 μs and the duty cycle is 50%. A single frequency signal at 17.5 GHz from a microwave signal generator (R&S SMA100B) is used to drive MZM1 to generate optical LO. By applying the EBPF mentioned above, channel-1 (16–17 GHz) and channel-3 (18–19 GHz) are realized. Then the single frequency signal is changed to 18.5 GHz to output channel-2 (17–18 GHz) and channel-4 (19–20 GHz). The outputs of all four channels are collected by a real-time oscilloscope (Keysight DSO9404A, Bandwidth: 4 GHz, Sampling rate: 20 GSa/s). The output waveforms are depicted in Fig. 5(a)–(d), with the corresponding time-frequency diagram shown in Fig. 5(e)–(h). As can be seen from Fig. 5(a)–(d), channel-1 to channel-4 outputs down-converted signals in the time domain in turn, which is consistent with the characteristic of the detected LFM signal.

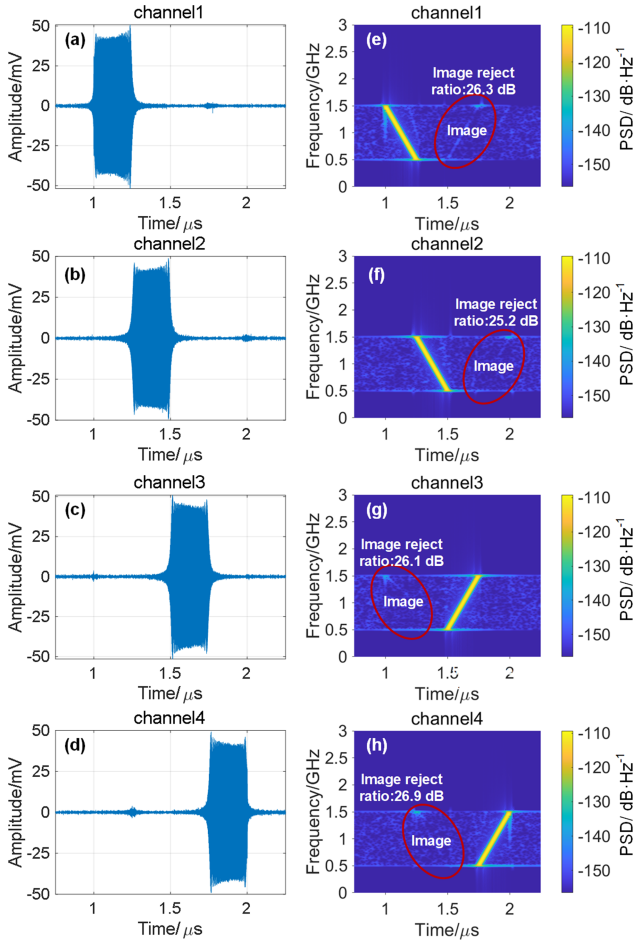

Fig. 5. Output 0.5–1.5 GHz IF signal waveforms of channel-1 to channel-4 (a)–(d) and corresponding frequency-time diagram (e)–(h).

In channel-1 and channel-2, because the frequency of detected LFM signals is lower than the LO, the results in the time-frequency diagram show that they have a negative chirp slope. The image frequency component with positive chirp slope is significantly suppressed. For channel-3 and channel-4, the Intermediate frequency (IF) LFM signals with positive chirp slope are retained, while the image frequency component with negative chirp is suppressed. The measured image-reject ratio of each channel is higher than 25.2 dB within the bandwidth of 1 GHz.

Therefore, the wideband LFM signal from 16 to 20 GHz can be successfully channelized into four consecutive channels with 1-GHz bandwidth.

C. AOA Measurement of Wideband RF Signals

By channelization, the wideband signal can be received by an ADC with lower bandwidth and sampling rate. After splicing the signals from different channels, the AOA of a wideband target can be calculated through the method mentioned in Part II. To investigate the feasibility of the proposed method, a target detection experiment is carried out.

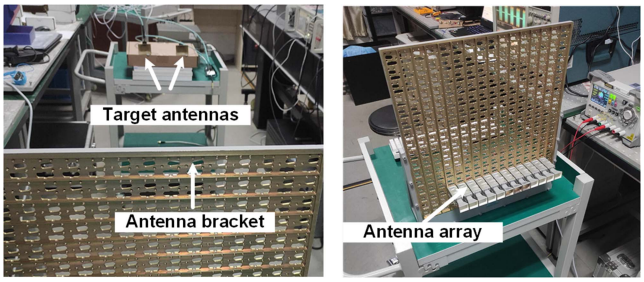

Fig. 6. Experiment setup of AOA measurement experiment (a) and picture of the receiver antenna array (b).

The setup of the AOA measurement experiment is depicted in Fig. 6(a), where two horn antennas are used as target signal sources. The antenna array used as receive array is shown in Fig. 6(b). The antenna array consists of 12 independent antenna units. Each antenna unit is integrated with a low noise amplifier. The spacing between two adjacent antennas is 2.46 cm. Before the AOA detection, a calibration procedure should be conducted first. Signals to be detected are directly connected to the modulator by RF cables, and then the VODLs are adjusted to eliminate the delay difference between the two receive links.

After calibration, a single target detection experiment is first carried out. The target source is first placed right in front of the antenna array with an AOA of 0° and a distance of 1.8 m. A wideband Gaussian noise signal with a center frequency of 19 GHz and a bandwidth of 2 GHz is used as the target signal. The measurement result is shown in Fig. 7(a). The AOA results obtained by both methods are 0.15°, which is close to the theoretical value. As can be seen, the pattern obtained by the traditional SAIR detection method in solid blue line has two grating lobes caused by the large element spacing, while in the result obtained by the wideband SAIR detection method, the grating lobe is significantly suppressed for over 60%. Then another wideband source covering 16–20 GHz is used as the target. The result is depicted in Fig. 7(b), the obtained AOA results are −0.09° for both methods, and a greater grating lobe suppression ratio of over 80% is achieved, which is better than the result of a 2 GHz bandwidth signal. This will be further analyzed in the discussion part.

Then, dual-target AOA detection is conducted. Two horn antennas are used as targets. Antenna 1 is placed at the reference point where AOA is 0°, and antenna 2 is placed 18 cm to the right of antenna 1, so the theoretical AOAs are 0° and 5.71°. The transmitted signals are incoherent Gaussian noises covering 16–20 GHz. The measurement result is shown in Fig. 8. The AOA results obtained by traditional SAIR in the solid blue line are −0.15° and 5.41°, while those obtained by the wideband SAIR detection method in the dashed orange line are −0.15° and 5.43°, respectively. We can see from the results that the grating lobes of both two targets are suppressed by over 70%.

To investigate that the proposed method can reduce the deterioration of AOA measurement results caused by system response under wideband conditions, we compare the AOA results before and after system response compensation. As is depicted in Fig. 9, compared with the results without compensation in the dotted

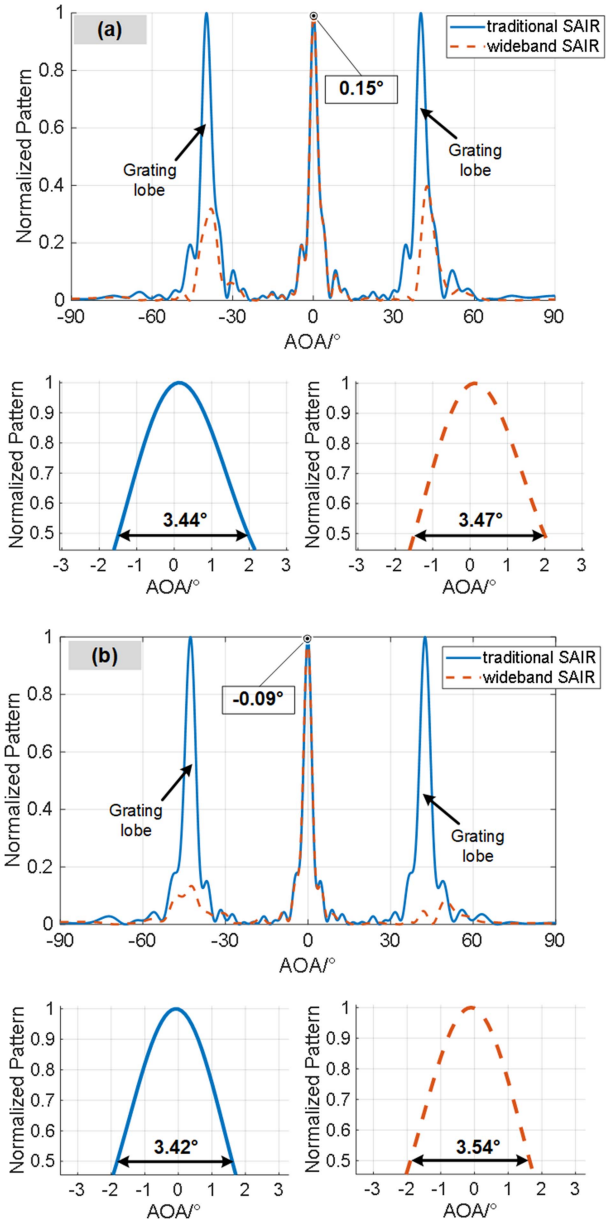

Fig. 7. AOA measurement results of a single target source covering 18–20 GHz (a) and a target source covering 16–20 GHz (b). Results obtained by the traditional SAIR detection method (solid blue line) and wideband SAIR detection method (dashed orange line).

blue line, the results after compensation have a higher grating lobe suppression ratio and the suppression ratio increases as the bandwidth increases.

The angular resolution of a 1-D linear array can be given by $0.89\lambda/L\cos\theta$, where λ is the wavelength at the center frequency, L is the length of the longest baseline, and θ is the AOA to be measured. In the AOA measurement experiment, signals received by 12 antennas are collected. The theoretical angular resolution at 0° can be calculated by $0.89\lambda\cdot 180°/n\pi d$, where, $n = 11$ is the number of baselines, and $d = 2.46$ cm is the element spacing. For the target source covering 18–20 GHz, the theoretical angular resolution is 2.98°. According to the 3-dB bandwidth of the pattern, the measured angular resolutions

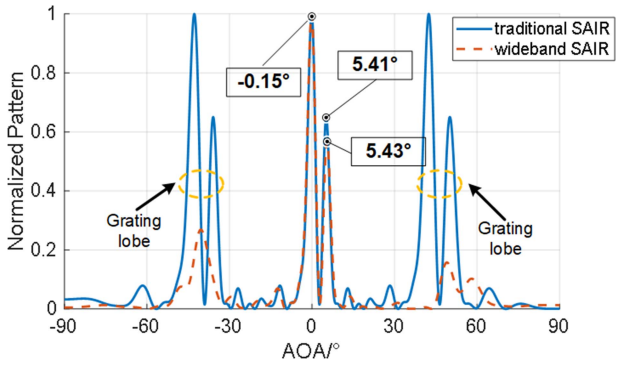

Fig. 8. AOA measurement results of dual target sources covering 16–20 GHz. Results obtained by the traditional SAIR detection method (solid blue line) and wideband SAIR detection method (dashed orange line).

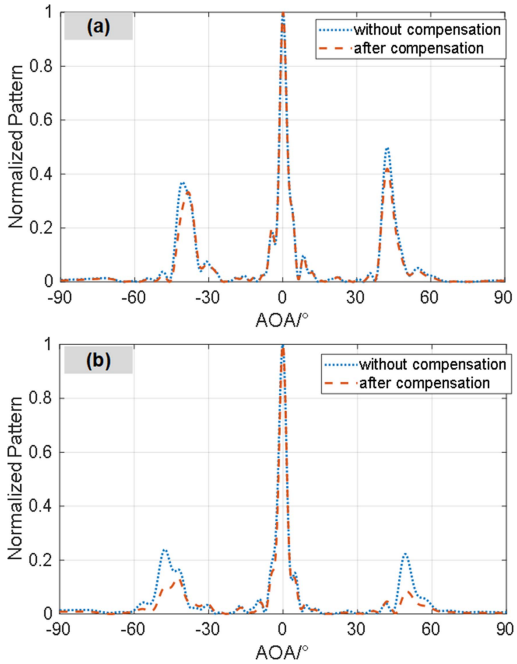

Fig. 9. AOA measurement results of a single target source covering 18–20 GHz (a) and a single target source covering 16–20 GHz (b). Results without compensating system response (dotted blue line) and after compensating system response (dashed orange line).

of the traditional SAIR detection method and wideband SAIR detection method are 3.44° and 3.47°, respectively. When it comes to the target source covering 16–20 GHz, the theoretical angular resolution is 3.14°, and the measured angular resolutions are 3.42° and 3.54°, respectively.

The reasons for the deterioration of AOA resolution in the experiment can be summarized into three parts. Firstly, due to the limitation of the experiment site, the far-field condition is not fully met, and the FOV of the receiving array antenna is relatively small. Therefore, the signal power collected by each antenna is different, which will lead to the widening of the main lobe. Secondly, the horn antennas used as targets cannot be equivalent to an ideal point target under the measurement range in the experiment. Finally, to simplify the analysis, the radiation

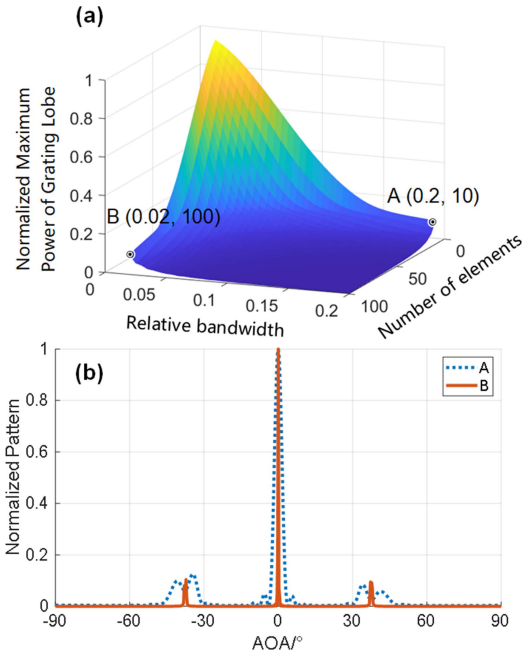

Fig. 10. The normalized maximum power of grating lobes under different bandwidths and number of elements (a). The simulated AOA measurement results in two extreme conditions at points A and B (b).

pattern of antenna elements is not considered in the experiment, which will also cause deterioration of the AOA measurement result [28].

IV. Discussion and Conclusion

In the experiment, the grating lobe suppression ratio of the AOA measurement result for the 4 GHz-bandwidth target source is obviously better than that for the 2 GHz-bandwidth target source. To further investigate the effect of target signal bandwidth and the number of array elements (baselines) on the grating lobe suppression ratio, we simulate the wideband SAIR detection of a point target source in the 0° direction of far-field under different bandwidths and the number of array elements. The transmitted signal is a bandpass Gaussian noise signal with the center frequency set to 20 GHz, and the array element spacing is 2.46 cm. The bandwidth of the target signal changes from 400 MHz to 4 GHz, while the number of elements varies from 10 to 100. The simulation results are summarized as a curved surface in Fig. 10(a). As can be seen, the increase of both bandwidth and the number of elements can degrade the power of the maximum grating lobe. The simulated AOA measurement results under two extreme conditions A and B are depicted in Fig. 10(b). As can be seen, the power of grating lobes is suppressed by nearly 90% in each result. What should be noted is that the grating lobe suppression achieved by the proposed method is realized based on the wideband characteristics of the detected signal itself, and only the 1-D uniform linear array is used. If it can be combined with some array arrangement optimization methods [29], a better grating lobe suppression result can be achieved.

In addition, since the signal of each antenna needs to be received, the MWP channelizer used here is still complicated

and bulky in practical applications. In the future, the simplification of the hardware structure can be mainly implemented from two aspects. Firstly, the integration of photonics devices is foreseeable, many components used in the MWP channelizer can be integrated [30], which may greatly reduce the cost and size of the photonics-assisted SAIR system. Secondly, sparse array and compressive coding algorithms can be applied to reduce the number of receiving chains in the SAIR system [28], which will further moderate the hardware complexity and cost. We are planning to carry out relevant research in our future works.

To conclude, we have proposed a photonics-assisted SAIR detection method for wideband RF source localization. By combining the principle of IAP in the wideband phased array system and CPS-based AOA measurement applied in the wideband sonar system, the proposed method can suppress the grating lobe caused by large array element spacing. A proof-of-concept experiment assisted by an MWP RF channelizer is conducted. With the proposed SAIR detection method, grating lobe suppressed AOA measurement of both single and double wideband RF targets is achieved. The proposed SAIR detection method can facilitate the research of wideband microwave/millimeter-wave array detection systems and provide a novel solution for both wideband communication and electronic warfare systems.

REFERENCES

[1] T. Luthi and C. Matzler, "Stereoscopic passive millimeter-wave imaging and ranging," *IEEE Trans. Microw. Theory Techn.*, vol. 53, no. 8, pp. 2594–2599, Aug. 2005.

[2] F. Liu et al., "Integrated sensing and communications: Towards dual-functional wireless networks for 6G and beyond," *IEEE J. Sel. Areas Commun.*, vol. 40, no. 6, pp. 1728–1767, Jun. 2022.

[3] D. K. Pin Tan et al., "Integrated sensing and communication in 6G: Motivations, use cases, requirements, challenges and future directions," in *Proc. IEEE 1st Int. Online Symp. Joint Commun. Sens.*, 2021, pp. 1–6.

[4] J. Capmany and D. Novak, "Microwave photonics combines two worlds," *Nature Photon.*, vol. 1, no. 6, pp. 319–330, Jun. 2007.

[5] G. Serafino et al., "Toward a new generation of radar systems based on microwave photonic technologies," *J. Lightw. Technol.*, vol. 37, no. 2, pp. 643–650, Jan. 2019.

[6] S. Pan and Y. Zhang, "Microwave photonic radars," *J. Lightw. Technol.*, vol. 38, no. 19, pp. 5450–5484, Oct. 2020.

[7] X. Zou, B. Lu, W. Pan, L. Yan, A. Stöhr, and J. Yao, "Photonics for microwave measurements," *Laser Photon. Rev.*, vol. 10, no. 5, pp. 711–734, Sep. 2016.

[8] P. Ghelfi et al., "A fully photonics-based coherent radar system," *Nature*, vol. 507, no. 7492, pp. 341–345, Mar. 2014.

[9] X. Zou, W. Li, W. Pan, B. Luo, L. Yan, and J. Yao, "Photonic approach to the measurement of time-difference-of-arrival and angle-of-arrival of a microwave signal," *Opt. Lett.*, vol. 37, no. 4, pp. 755–757, Feb. 2012.

[10] Z. Cao, H. P. A. van den Boom, R. Lu, Q. Wang, E. Tangdiongga, and A. M. J. Koonen, "Angle-of-arrival measurement of a microwave signal using parallel optical delay detector," *IEEE Photon. Technol. Lett.*, vol. 25, no. 19, pp. 1932–1935, Oct. 2013.

[11] H. Chen and E. H. W. Chan, "Angle-of-arrival measurement system using double RF modulation technique," *IEEE Photon. J.*, vol. 11, no. 1, Feb. 2019, Art. no. 7200110.

[12] H. Chen and E. H. W. Chan, "Simple approach to measure angle of arrival of a microwave signal," *IEEE Photon. Technol. Lett.*, vol. 31, no. 22, pp. 1795–1798, Nov. 2019.

[13] H. Chen and E. H. W. Chan, "Photonics-based CW/pulsed microwave signal AOA measurement system," *J. Lightw. Technol.*, vol. 38, no. 8, pp. 2292–2298, Apr. 2020.

[14] P. Li et al., "Angle-of-arrival estimation of microwave signals based on optical phase scanning," *J. Lightw. Technol.*, vol. 37, no. 24, pp. 6048–6053, Dec. 2019.

[15] B. Vidal, M. A. Piqueras, and J. Marti, "Direction-of-arrival estimation of broadband microwave signals in phased-array antennas using photonic techniques," *J. Lightw. Technol.*, vol. 24, no. 7, pp. 2741–2745, Jul. 2006.

[16] J. Cai, X. Chang, W. Liu, T. Shang, and C. Li, "Photonic direction-of-arrival estimation based on compressive sensing," *Appl. Opt.*, vol. 60, no. 12, pp. 3482–3486, Apr. 2021.

[17] S. Li, H. Cao, and X. Zheng, "Concurrent photonic measurement of angle-of-arrival and chirp rate of microwave LFM signal," *Chin. Opt. Lett.*, vol. 18, no. 12, Dec. 2020, Art. no. 123902.

[18] Y. Yang et al., "Photonics-based simultaneous angle of arrival and frequency measurement system with multiple-target detection capability," *J. Lightw. Technol.*, vol. 39, no. 24, pp. 7656–7663, Dec. 2021.

[19] J. Murakowski, G. J. Schneider, S. Shi, C. A. Schuetz, and D. W. Prather, "Photonic probing of radio waves for k-space tomography," *Opt. Exp.*, vol. 25, no. 14, pp. 15746–15759, Jul. 2017.

[20] C. J. Ryan, D. D. Ross, J. Murakowski, G. J. Schneider, and D. W. Prather, "Kalman-filter accelerated k-space tomography," *J. Lightw. Technol.*, vol. 37, no. 3, pp. 942–948, Feb. 2019.

[21] D. J. Brady, *Optical Imaging and Spectroscopy*. Hoboken, NJ, USA: Wiley, 2009.

[22] A. R. Thompson, J. M. Moran, and G. W. Swenson Jr, *Interferometry and Synthesis in Radio Astronomy*. Berlin, Germany: Springer Nature, 2017.

[23] X. Bosch-Lluis, I. Ramos-Perez, A. Camps, N. Rodriguez-Alvarez, E. Valencia, and H. Park, "Common mathematical framework for real and synthetic aperture by interferometry radiometers," *IEEE Trans. Geosci. Remote Sens.*, vol. 52, no. 1, pp. 38–50, Jan. 2014.

[24] X. Ye, D. Zhu, Y. Zhang, S. Li, and S. Pan, "Analysis of photonics-based RF beamforming with large instantaneous bandwidth," *J. Lightw. Technol.*, vol. 35, no. 23, pp. 5010–5019, Dec. 2017.

[25] R. Rotman, O. Raz, S. Barzilay, S. R. Rotman, and M. Tur, "Wideband antenna patterns and impulse response of broadband RF phased arrays with RF and photonic beamforming," *IEEE Trans. Antennas Propag.*, vol. 55, no. 1, pp. 36–44, Jan. 2007.

[26] W. Guo, S. Piao, J. Guo, Y. Lei, and K. Iqbal, "Passive detection of ship-radiated acoustic signal using coherent integration of cross-power spectrum with doppler and time delay compensations," *Sensors*, vol. 20, no. 6, Mar. 2020, Art. no. 1767.

[27] W. Chen, D. Zhu, C. Xie, J. Liu, and S. Pan, "Microwave channelizer based on a photonic dual-output image-reject mixer," *Opt. Lett.*, vol. 44, no. 16, pp. 4052–4055, Aug. 2019.

[28] E. Kpre, C. Decroze, M. Mouhamadou, and T. Fromenteze, "Computational imaging for compressive synthetic aperture interferometric radiometer," *IEEE Trans. Antennas Propag.*, vol. 66, no. 10, pp. 5546–5557, Oct. 2018.

[29] D. Zhang, F. Zhang, and S. Pan, "Grating-lobe-suppressed optical phased array with optimized element distribution," *Opt. Commun.*, vol. 419, pp. 47–52, Jul. 2018.

[30] G. Hu et al., "Optical beamformer based on diffraction order multiplexing (DOM) of an arrayed waveguide grating," *J. Lightw. Technol.*, vol. 37, no. 13, pp. 2898–2904, Jul. 2019.